Materials Chemistry and Physics 242 (2020) 122075

Contents lists available at ScienceDirect

Materials Chemistry and Physics

journal homepage: www.elsevier.com/locate/matchemphys

Compositional effects on the electrical properties of extremely disordered molybdenum oxynitrides thin films

J.A. Hofer [a,*], S. Bengio [b], G. Rozas [a,b], P.D. Pérez [b], M. Sirena [a,b], S. Suárez [a,b], N. Haberkorn [a,b]

[a] Instituto Balseiro, Universidad Nacional de Cuyo and Comisión Nacional de Energía Atómica, Av. Bustillo 9500, 8400, San Carlos de Bariloche, Argentina
[b] Comisión Nacional de Energía Atómica and Consejo Nacional de Investigaciones Científicas y Técnicas, Centro Atómico Bariloche, Av. Bustillo 9500, 8400, San Carlos de Bariloche, Argentina

HIGHLIGHTS

- Molybdenum oxynitride thin films were grown by reactive sputtering.
- Electrical transport properties depend on the stoichiometry.
- Nitrogen-rich films are superconducting.
- Oxygen-rich films display semiconductor-like behavior.

ARTICLE INFO

Keywords:
Molybdenum
Oxynitrides
Thin films
Sputtering
Electrical transport

ABSTRACT

Molybdenum oxynitride (MoN_xO_y) thin films were grown by reactive sputtering on Si (100) substrates at room temperature. The partial pressure of Ar was fixed at 90%, and the remaining 10% was adjusted with mixtures N_2: O_2 (varying from pure N_2 to pure O_2). The electrical properties of the films depend on the chemical composition. Thin films grown using mixtures up to 2% O_2 have γ-Mo_2N phase and display superconductivity. The superconducting critical temperature T_c reduces from ~6.8 K to below 3.0 K as the oxygen increases. On the other hand, the films are mostly amorphous for gas mixtures above 2% O_2. The electrical conductivity shows a semiconductor-like behavior well described by variable-range hopping conduction. The analysis of the optical properties reveals that the samples do not have a defined semiconductor bandgap, indicating that the high structural disorder produces electron excitation for a wide range of energies.

1. Introduction

There is currently great interest in the synthesis of thin films at low temperatures for the development of electronic devices on flexible substrates [1,2]. Superconducting transition metal nitride films deposited at room temperature usually display high chemical stability and sharp transitions [3–5]. Oxygen addition expands the physical properties of these materials [6]. Oxynitrides – depending on the nitrogen/oxygen ratio – are between metallic nitrides and resistive oxides. The study of the change of the properties with doping is interesting to tune intermediate states, and in other cases, generate new ones. For example, the addition of oxygen suppresses the superconductivity in TiN_yO_y [7,8]. On the other hand, new superconducting phases emerge in NbN_yO_y for an adequate amount of oxygen [9].

Molybdenum oxynitrides thin films may have potential technological applications due to the attractive properties displayed by oxides and nitrides. The most common molybdenum oxides are the monoclinic dioxide (MoO_2) and the trioxide (MoO_3). MoO_2 exhibits unusual properties among oxides, shifting from one with metallic properties into a semiconductor when the structural disorder increases [10–12]. MoO_3 is a wide-band-gap semiconductor [13,14]. Molybdenum nitrides display several superconducting crystalline phases: γ-Mo_2N (cubic) with a superconducting critical temperature T_c~ 5 K [15], β-Mo_2N (tetragonal) with T_c ~ 5 K [16] and δ-MoN (hexagonal) with T_c ~ 12 K [17]. The chemical composition of molybdenum nitride thin films grown by reactive sputtering can be adjusted by the gas mixture [18]. Moreover, disorder at the nanoscale increases the T_c in γ-Mo_2N thin films from ≈5 K to 8 K [19]. Despite the interesting properties displayed by the nitrides and oxides, there are only a few studies on the electrical properties of molybdenum oxynitrides [20,21].

* Corresponding author.
E-mail address: juan.hofer@cab.cnea.gov.ar (J.A. Hofer).

https://doi.org/10.1016/j.matchemphys.2019.122075
Received 22 May 2019; Received in revised form 26 July 2019; Accepted 27 August 2019
Available online 5 September 2019

In this work, we analyze the influence of the reactive gas mixture on the compositional, structural, and electrical properties of molybdenum oxynitrides thin films grown at room temperature by reactive sputtering on Si (100) substrates. The partial pressure of Ar was fixed at 90%, and the remaining 10% was adjusted with mixtures N_2: O_2 (varying from pure N_2 to pure O_2). The electrical resistivity of the films is analyzed by considering the chemical doping and the structural disorder.

2. Material and methods

Molybdenum oxynitride films were deposited by DC reactive magnetron sputtering on Si (100) (typical size 1 cm^2). No intentional heating of the substrate was used. The base pressure in the chamber was 1.3×10^{-4} Pa. Films were grown from a pure Mo target (diameter 3.8 cm) in a reactive Ar:N_2:O_2 mixture. The target power and the total pressure were fixed at 50 W and 0.67 Pa, respectively. The substrate was positioned directly over the target at ≈ 5.5 cm. Reactive sputtering was performed with 90% Ar and 10% of a N_2:O_2 mixture (with O_2 total fraction 0, 1%, 2%, 3.3%, 5%, 6.6% and 10%). The notation [MoN_xO_y] indicates thin films growth in a N_2:O_2 gas mixture where x and y are the respective percentages.

X-ray diffraction (XRD) data was obtained using a Panalytical Empyrean equipment operated at 40 kV and 30 mA with the $Cu_{K\alpha}$ radiation. The structural analysis was performed based on Θ-2Θ scans with an angular resolution of 0.02°. The film thickness was measured by low-angle X-ray reflectivity (XRR). Surface images were obtained in a Zeiss Gemini scanning electron microscope (SEM). Atomic force microscopy (AFM) measurements were performed in a Dimension 3100 ©Brucker microscope. The AFM images presented in this work were performed in tapping mode. RMS values were estimated from the root mean square average of height deviation taken from the mean image data plane. The chemical stoichiometry of the films was analyzed by Rutherford Backscattering Spectroscopy (RBS) with a TANDEM (NEC, 1.7 MV) accelerator using a 2 MeV $^4He^{2+}$ ion beam. Surface composition analysis was performed by X-ray photoelectron spectroscopy (XPS) using a standard Al/Mg twin-anode X-ray gun and a hemispherical electrostatic electron energy analyzer (high vacuum conditions with a base pressure of 10^{-9} Torr).

The optical parameters of [$MoN_{6.6}O_{3.3}$], [$MoN_{3.3}O_{6.6}$], and [MoN_0O_{10}] were deduced from spectroscopic ellipsometry measurements (Ψ and Δ) carried out in the spectral region of 200–1200 nm using a Woollam NIR-Vis-UV ellipsometer in three different angles of incidence: 61°, 66° and 71°. The data was analyzed using the manufacturer's code. The electrical transport measurements were performed using the standard four-point configuration.

3. Results and discussion

The thicknesses of the films were determined from XRR. The modulation in the Θ-2Θ scans is related to the thickness d of the film as:

$$sin^2\theta = \left[\frac{(n+K)\lambda}{2d}\right]^2 + 2\delta, \quad (1)$$

where 1-δ is the real part of the index of refraction of the film, λ is the x-ray wavelength, and a value of $k = 0$ corresponds to an intensity minimum and $k = ½$ to an intensity maximum [22]. Fig. 1*a* shows $sin^2\theta - vs - n^2$ for the low angle minima of films grown 5 min using different gas mixtures. Inset Fig. 1*a* shows the XRR data for [$MoN_{10}O_0$]. Fig. 1*b* shows total thickness as function of the gas mixture. The film thicknesses are 80 nm for [$MoN_{10}O_0$], 84 nm for [MoN_9O_1], 96 nm for [MoN_8O_2], 136 nm for [$MoN_{6.6}O_{3.3}$], 140 nm for [MoN_5O_5] (interpolated) 145 nm for [$MoN_{3.3}O_{6.6}$], and 145 nm for [MoN_0O_{10}]. The results indicate that the growth rate for [$MoN_{10}O_0$] is 16 nm/min. The value rises gradually as the oxygen in the mixture increases showing a clear crossover at ≈ 2% O_2. Finally, the growth rate for ≈10% O_2 (no N_2) is 28 nm/min. The

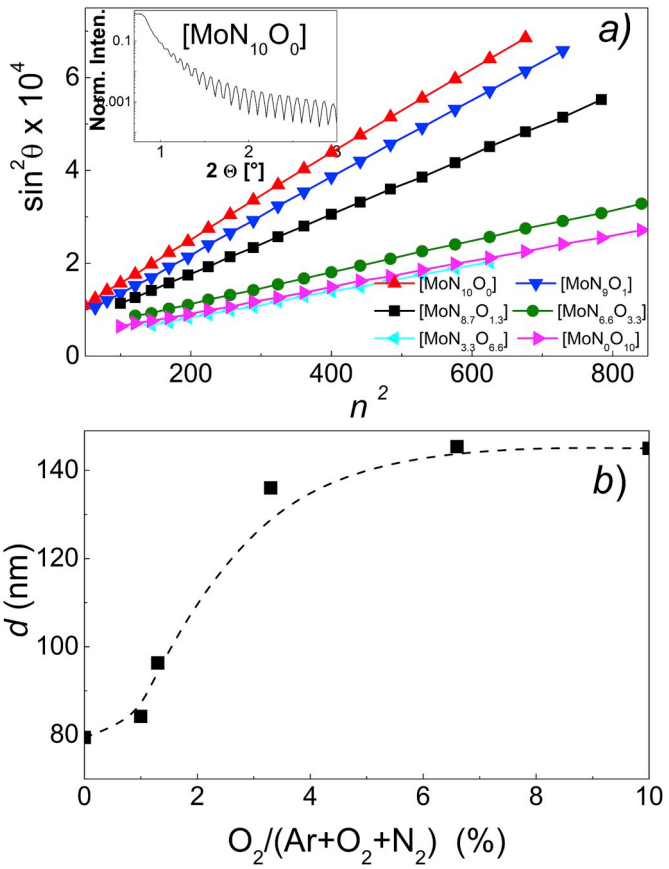

Fig. 1. *a)* $sin^2\theta - vs - n^2$ for the minima in the XRR data. Solid line is the least-squares linear fit to the data. Inset: typical XRR data for [$MoN_{10}O_0$] (Normalized Intensity vs. 2Θ). *b*) Thickness for films grown during 5 min using different gas mixtures. The data is calculated from the slope of *a)*.

differences in the sputtering rate may be related to the surface passivation of the target by nitrides and oxides [23]. Considering the potential applications of oxynitrides in electronic devices, we analyze the surface of the films using both SEM and AFM images. The analysis of the surface indicates that the roughness is weakly affected by the gas mixture. Fig. 2 shows typical images for the extremes [$MoN_{10}O_0$] and [MoN_0O_{10}]. The surfaces are extremely flat and free of morphological defects. The films display very smooth surfaces with Root Mean Square (RMS) roughness smaller than 0.5 nm.

Fig. 3 shows the XRD patterns for molybdenum oxynitride films. Nitrogen-rich films display diffractions corresponding to the γ-Mo_2N phase (JCPDS 03–0907) [23]. For gas mixtures up to 1% O_2, the films are textured along the (200). The diffractions (111) and (200) are observed in [MoN_8O_2]. Gas mixtures above 2% O_2 produce mainly amorphous films, which is evident from the absence of peaks in the XRD patterns. Even for 10% O_2, no features related to molybdenum oxides are observed (JCPDS 032–0671 for MoO_2 and JCPDS 021–0569 for MoO_3). The change in the microstructure from nanocrystalline Mo_2N phase to an amorphous phase is coherent with the increment in the growth rate described earlier. In order better to understand the influence of the stoichiometry on the structural changes, we study the chemical composition by RBS (see Table 1). The error bar for the data is 5%. The extremes [$MoN_{10}O_0$] and [MoN_0O_{10}] correspond to $Mo_2N_{1.1}$ and MoO_2, respectively. The data show that for gas mixtures above 2% O_2, the amount of nitrogen drops and the samples are mainly oxides. This crossover in the chemical composition is in agreement with the presence of amorphous structures in the XRD data.

XPS analysis was employed to investigate the electronic structure of the pristine and cleaned films. The surface cleaning was performed with

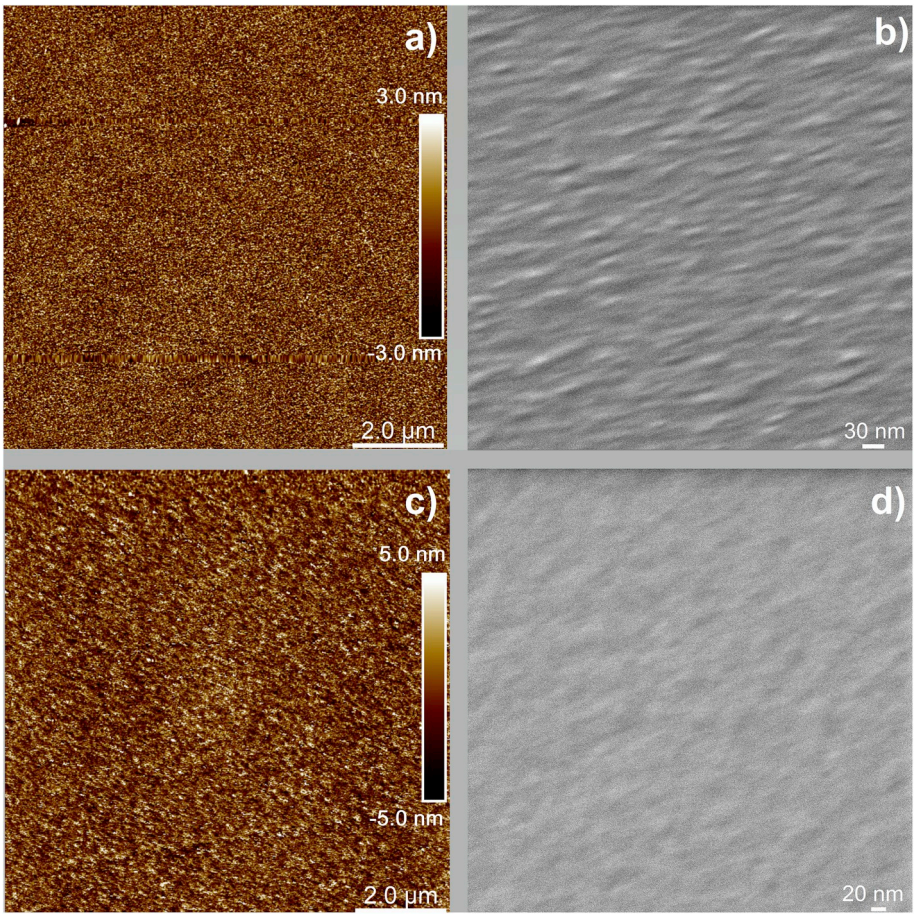

Fig. 2. AFM and SEM images, respectively, for: *a-b*) $[MoN_{10}O_0]$ and *c-d)* $[MoN_0O_{10}]$.

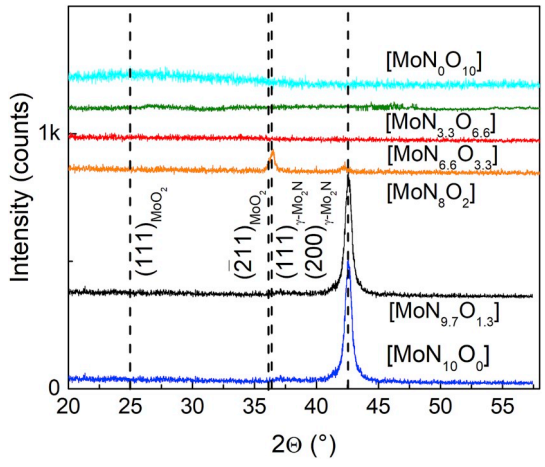

Fig. 3. XRD patterns for molybdenum oxynitride films.

Ar^+ sputtering (2 kV). The pristine films display a component at binding energy (BE) ≈ 232.7 eV related to superficial MoO_3 that is removed during the sputtering process [24]. Fig. 4 shows the XPS spectra in the Mo*3d* region for cleaned $[MoN_{10}O_0]$, $[MoN_8O_2]$, $[MoN_5O_5]$ and $[MoN_0O_{10}]$. The results can be divided into nitrides and oxides. The spectra for $[MoN_{10}O_0]$ and $[MoN_8O_2]$ display the Mo_2N component (binding energy BE ≈ 228.5 eV) shifted to smaller BE by ≈ 0.2 eV (see top curves in Fig. 4). The pristine films grown with gas mixtures above 2% O_2 display the MoO_2 with BE ≈ 229.3 eV (not shown). After clean the surface, $[MoN_5O_5]$ and $[MoN_0O_{10}]$ suffer a drastic reduction showing MoO and metallic Mo (see bottom curves in Fig. 4) [25–27].

Table 1
Chemical composition (atomic (%)) obtained from RBS measurements. The error bars for the data are estimated in approximately 5%.

Sample	Mo	N	O
$[MoN_{10}O_0]$	0.64	0.36	–
$[MoN_9O_1]$	0.54	0.34	0.12
$[MoN_8O_2]$	0.53	0.3	0.17
$[MoN_{6.6}O_{3.3}]$	0.34	0.26	0.40
$[MoN_5O_5]$	0.40	0.24	0.36
$[MoN_{3.3}O_{6.6}]$	0.40	0.24	0.35
$[MoN_0O_{10}]$	0.33	–	0.67

To understand in more detail the electronic structure of the films, we analyzed its valence band spectra. The comparison between $[MoN_{10}O_0]$ and $[MoN_8O_2]$ indicates that for the same contribution of N2s, the first displays a higher O2s intensity (see top curves in Fig. 5). $[MoN_8O_2]$ displays a larger contribution of the metallic Mo*4d*. The latter is also observed at $[MoN_5O_5]$ and $[MoN_0O_{10}]$ (see bottom curves in Fig. 5). The contribution of nitrogen drops as the oxygen increases. Nitrides are more stables than oxides to the sputtering process. No nitrogen vacancies are formed during the sputtering process used to clean the surface in $[MoN_{10}O_0]$. While oxygen vacancies are formed in $[MoN_5O_5]$ and $[MoN_0O_{10}]$ (see inset Fig. 5). The spectrum for $[MoN_8O_2]$ suggests that the sample is affected by the creation of oxygen and presumably nitrogen vacancies. This supposition explains the shift in the Mo3d spectra and the rise in the Mo4d intensity relative to the O1s and N1s. Furthermore, the width of the Mo4d peak and its proximity to the N2p orbital reveals a high hybridization, while the narrow Mo4d peak and its

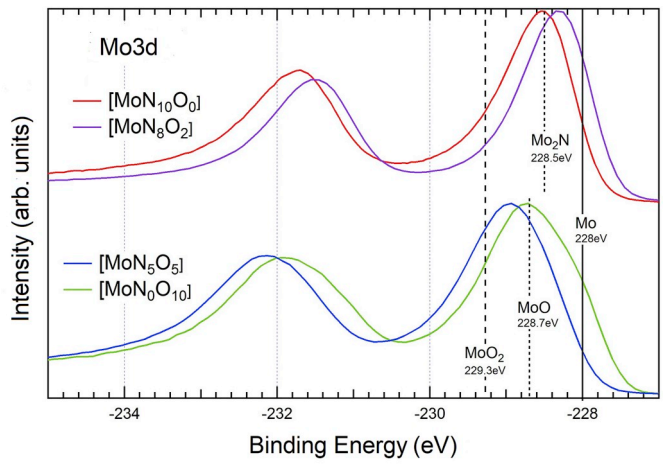

Fig. 4. XPS Mo3d spectra for $[MoN_{10}O_0]$, $[MoN_8O_2]$, $[MoN_5O_5]$ and $[MoN_0O_{10}]$. The data correspond to films with a clean surface.

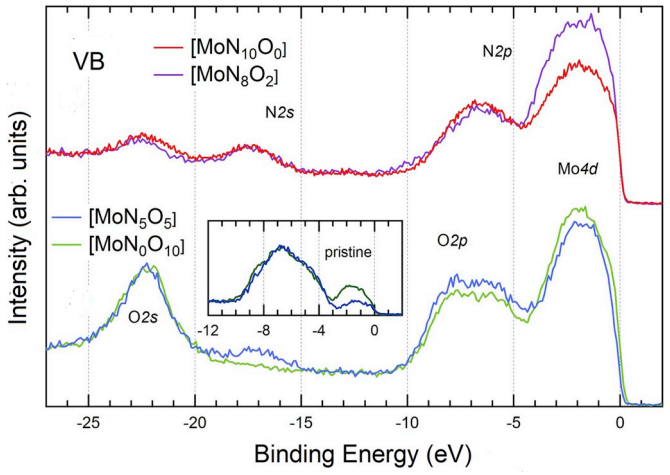

Fig. 5. XPS valence band (VB) spectra for surface cleaned $[MoN_{10}O_0]$, $[MoN_8O_2]$, $[MoN_5O_5]$ and $[MoN_0O_{10}]$. Inset shows the spectra for pristine $[MoN_5O_5]$ and $[MoN_0O_{10}]$.

distancing with the O2p orbital indicate lower hybridization.

To correlate the microstructure and the electronic properties, we measured the electrical resistivity versus temperature for the different films (see Fig. 6). The results show that films with reactive mixtures up to 2% O_2 display superconductivity (see Fig. 6a). The T_c decreases from ≈6.8 K for $[MoN_{10}O_0]$ to ≈ 3 K for $[MoN_8O_2]$ (see Figs. 6b and 6c). Thin films grown using mixtures above 3.3% O_2 display a semiconductor-like behavior. The measured resistivities at 273 K were found to $\rho^{273\,K} = 100$ (20) μΩ.cm for $[MoN_{10}O_0]$, 140 (20) μΩ.cm for $[MoN_9O_1]$, 180 (20) μΩ.cm for $[MoN_8O_2]$, 200 (20) μΩ.cm for $[MoN_{6.6}O_{3.3}]$, 250 (20) μΩ.cm for $[MoN_5O_5]$, 700 (20) μΩ.cm for $[MoN_{3.3}O_{6.6}]$, and 1500 (50) μΩ.cm for $[MoN_0O_{10}]$, Following, the influence of the oxygen impurities in the superconducting properties is analyzed by measuring the upper critical field (H_{c2}). The temperature dependence of H_{c2} for dirty superconductors is described by the Werthamer-Helfand-Hohenberg (WHH) formula [28]:

$$ln\frac{1}{t} = \sum_{v=-\infty}^{\infty}\left(\frac{1}{|2v+1|} - \left[|2v+1| + \frac{\hbar}{t} + \frac{(\alpha\hbar/t)^2}{|2v+1| + (\hbar+\lambda_{so})/t}\right]^{-1}\right), \qquad (2)$$

where $t = T/T_c$, $\hbar = (4/\pi^2)(H_{c2}(T)/|dH_{c2}/dT|_{T_c})$, α is the Maki parameter, and λ_{so} is the spin-orbit scattering constant. When $\lambda_{so} = 0$, $H_{c2}(0)$

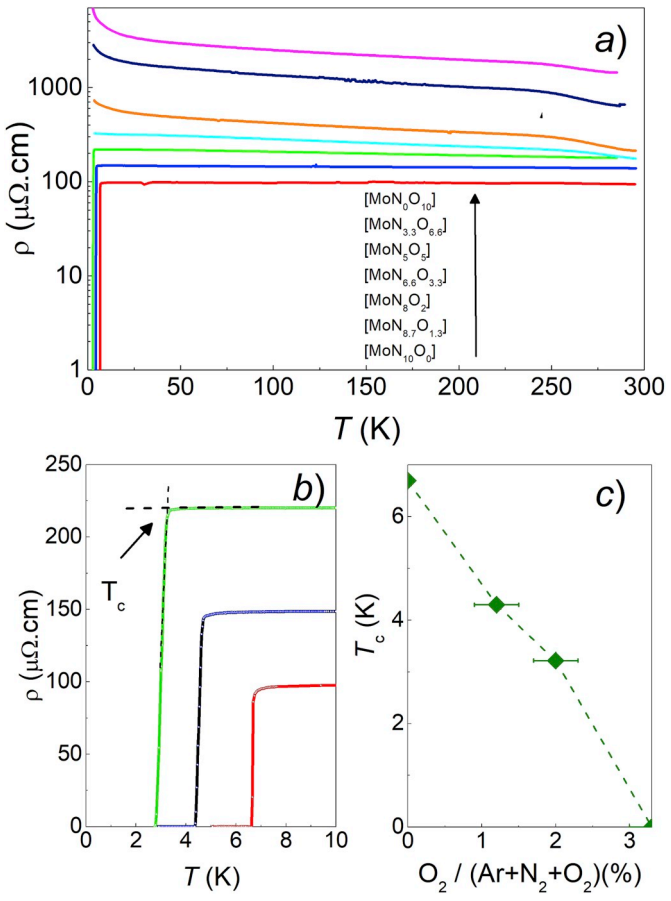

Fig. 6. *a)* Electrical resistivity versus temperature for molybdenum oxynitride films grown using different gas mixtures. *b)* Normalized resistance vs. temperature at $T < 10$ K for superconducting samples. *c)* T_c versus oxygen concentration in the reactive mixture.

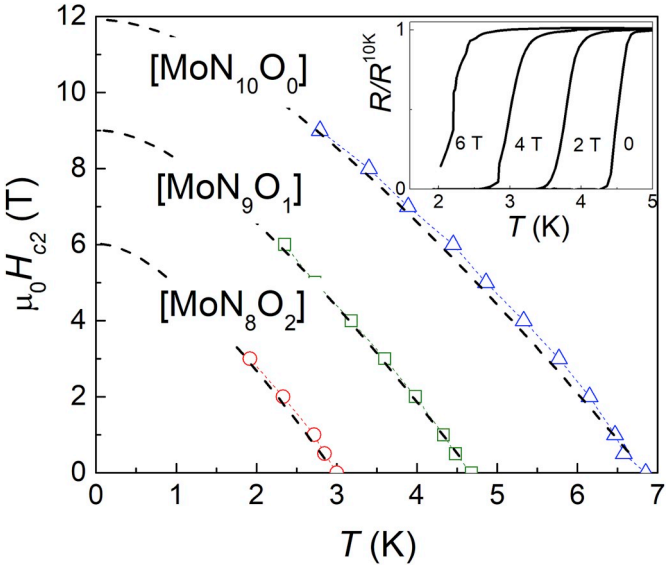

Fig. 7. Temperature dependence of the upper critical field (H_{c2}) for $[MoN_{10}O_0]$, $[MoN_9O_1]$ and $[MoN_8O_2]$. Inset shows typical curves of the resistance for different applied magnetic fields for $[MoN_9O_1]$.

obtained from the WHH formula satisfies the relation $H_{c2}(0) = \frac{H_{c2}^{orb}(0)}{\sqrt{1+\alpha^2}}$ [29]. Fig. 7 shows experimental data for $H_{c2}(T)$ and the fits using eq. (2). The inset in Fig. 7 shows typical curves of normalized resistance versus temperature for different magnetic fields in [MoN_9O_1]. The experimental data is well described by the WHH model using $\alpha = 0$ and $\lambda_{so} = 0$ (see dashed lines in Fig. 7). The obtained H_{c2} (0) values are 12 T for [$MoN_{10}O_0$], 9 T for [MoN_9O_1] and 6 T for [MoN_8O_2]. The coherence length ξ (0) values can be estimated using $\xi(0) = \sqrt{\Phi_0/(2\pi H_{c2}^{||}(0)}$ (with $\Phi_0 = 2.07 \times 10^{-7}$ G cm^2 is the flux quantum). The obtained ξ (0) values are 5.2 nm for [$MoN_{10}O_0$], 6 nm for [MoN_9O_1] and 7.4 nm for [MoN_8O_2]. It is important to note that for a weakly coupled BCS superconductor with similar band structure $\xi_0 = 0.18\frac{\hbar v_F}{k_B T_c}$ (v_F: Fermi velocity and k_B the Boltzmann constant) [30]. The $\xi_0{}^*T_c$ value for the different films decreases as the oxygen increases, suggesting modifications in the band structure.

Now we will analyze the semiconductor-like behavior for [MoN_5O_5], [$MoN_{3.3}O_{6.6}$], and [MoN_0O_{10}] in more detail. In general, the temperature dependence of the resistivity in disordered systems and amorphous semiconductors takes the following form:

$$\rho \approx \rho_0 \exp\left[-\left(\frac{T_0}{T}\right)^p\right], \quad (3)$$

where ρ_0 is a prefactor, T_0 is a characteristic temperature and the exponent p depends on the shape of the density of states at the Fermi level (FL) [31]. For Mott variable range hopping (VHR) p can be ¼ (3D systems) or 1/3 (2D systems). Moreover, $p = ½$ is expected for 2D systems in which the Coulomb interaction is important. Fig. 8 shows ln (ρ) vs. $T^{-1/4}$ for the analyzed samples. Straight lines are observed at low temperatures. To verify 3D VRH at low temperatures with $p = 1/4$, the equation [3] can be rewritten as $W = -\delta(ln\sigma(T))/\delta(lnT) = p\left(T_0/T\right)^p$ [32]. Inset Fig. 8 shows lnW versus lnT for [$MoN_{3.3}O_{6.6}$], the slope $p = 0.24$ (0.01) confirms the mechanism. The T_0 values obtained from the slopes are 1.4 K, 4.5 K and 25 K, for [MoN_5O_5], [$MoN_{3.3}O_{6.6}$], and [MoN_0O_{10}], respectively. From the values of T_0 it is possible to estimate the hopping energy $E_h(T)$ for a given temperature T [33]:

$$E_h(T) = \frac{1}{4}k_B T^{3/4} T_0^{1/4} \quad (4)$$

The E_h (5 K) goes from 100 μeV to 160 μeV as the oxygen increases. These values are much smaller than those usually observed for more insulating samples such as manganites and ZnO [39 [34]].

The semiconductor-like behavior in the samples was analyzed by ellipsometry measurements. Refractive index (n) and extinction coefficient (k) were calculated from the modeling of the ellipsometric variables (Ψ and Δ). Fig. 9a shows the results for wave lengths λ between 200 nm and 1200 nm for [MoN_5O_5], [$MoN_{3.3}O_{6.6}$] and [MoN_0O_{10}]. The refraction index increases monotonically as the energy decreases. Moreover, K (λ) is different from the dependence expected for semiconductors with a defined band gap. There is not a crossover to lower absorption when the energy decreases. For amorphous semiconductors, there is not long range atomic order. However, the short-range order remains to some extent, giving rise thereby to a band-like structure of electron energy states similar to that of crystalline semiconductors. Nevertheless, the absorption edge becomes indistinguishable due to the high disorder. To verify the presence of a gap when the disorder is reduced, [MoN_0O_{10}] was annealed at 600 °C for 1 h using a vacuum of 1.3×10^{-4} Pa (sample 1) and 101325 Pa O_2 (sample 2). Fig. 9b shows the n (λ) and the K (λ) dependences after annealing. The latter displays a strong decrease in the visible and near-infrared (NIR) range in agreement with the expectations for semiconductors. In the case of the oxygen-annealed sample, we cannot estimate reliable optical properties because the small absorption and thickness of the annealed material difficult the fitting of the ellipsometric optical model. In fact, the

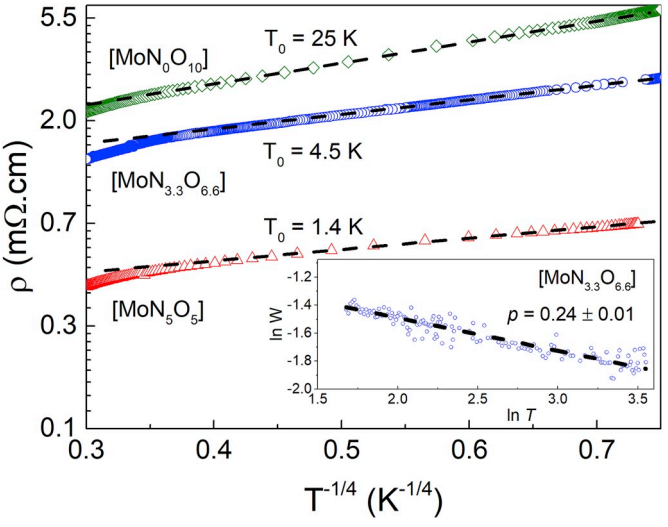

Fig. 8. ln ρ vs $T^{-1/4}$ for [MoN_5O_5], [$MoN_{3.3}O_{6.6}$] and [MoN_0O_{10}]. The inset shows ln W vs ln T for [$MoN_{3.3}O_{6.6}$] (with $W = -\delta(ln\sigma(T))/\delta(lnT)$).

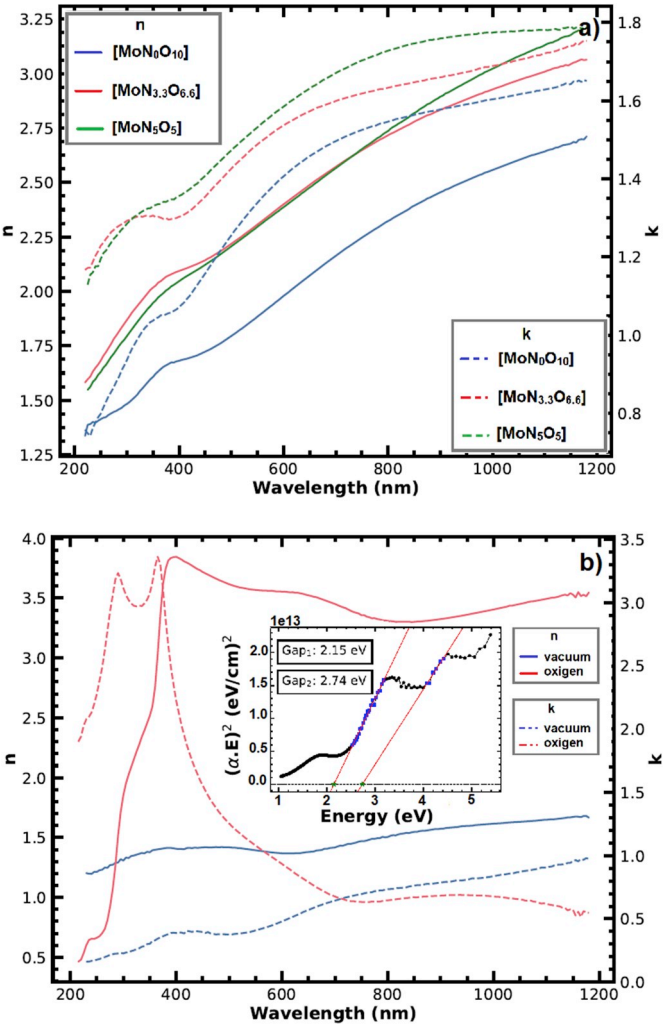

Fig. 9. Wavelength dependence of the refractive index (n) and extinction coefficient (k) of: *a)* as-deposited [MoN_5O_5], [$MoN_{3.3}O_{6.6}$] and [MoN_0O_{10}]; *b)* [MoN_0O_{10}] annealed at 600 °C in vacuum and under 101325 Pa O_2. Inset shows $(\alpha h\nu)^2$ vs. hν for vacuum-annealed [MoN_0O_{10}].

obtained n and k values are greatly influenced by the optical properties of the Si substrate. For the vacuum-annealed sample, however, we can estimate a band gap using an $(\alpha h\nu)^2$ vs. $(h\nu)$ plot (with $\alpha = 4\pi k/\lambda$) [11, 35]. Inset Fig. 9b shows the obtained results for annealed [MoN_0O_{10}]. The curve shows multiple steps, indicating different oxidation states for Mo [35]. At least two different band gaps can be identified, showing that the thermal annealing increases the order and reduces the metallic behavior. The film annealed in vacuum display energy gap values of ≈2.15 eV and ≈2.74 eV. The values are in the range of those previously reported for MoO_2 and MoO_3 [11,35]. As we mentioned earlier, the presence of more than one gap may be related to disorder and changes in oxygen stoichiometry. Similar features have been previously observed in thermal annealed Mo oxide thin films obtained by electrodeposition [11].

4. Conclusions

In summary, we analyzed the influence of the chemical composition on the structural and electronic properties of molybdenum oxynitrides thin films grown by reactive sputtering on Si (100) substrates at room temperature. The electronic properties of the films are affected by the composition of the reactive gas mixture. For rich N_2, the films are superconducting. The T_c is systematically reduced from ≈6.8 K for Mo-64 *at.*% N-36 *at.*% to ≈3 K for Mo-53 at.%N-30 *at.*% O-17 *at.*%. The oxygen is an interstitial impurity in the superconducting γ-Mo_2N phase and is also segregated as amorphous MoO_2. For rich O_2 mixtures, the films are mainly amorphous oxide and display a semiconductor-like behavior. The electrical resistivity depends on the oxygen content. The electrical transport shows a semiconductor-like behavior with a VRH conduction at low temperatures. The analysis of the optical properties reveals that the samples do not have a defined semiconductor bandgap, indicating that the high structural disorder produces electron excitation for a wide range of energies. Further investigations on the influence of the thermal annealing on the electronic should contribute to understanding the role of the disorder on the resulting electronic properties.

Declarations of interest

None.

Acknowledgments

The authors thank Bernardo Pentke for technical assistance. This work was partially supported by the ANPCyT (PICT 2015-2171), U. N. de Cuyo 06/C505 and CONICET PIP 2015-0100575CO. JAH, SB, GR, MS and NH are members of the of the Instituto de Nanociencia y Nanotecnología, CNEA-CONICET.

References

[1] B. Walter, C. Bockstiegel, B.A. Mazin, M. Daal, Laminated NbTi-on-kapton microstrip cables for flexible sub-kelvin RF electronics, IEEE Trans. Appl. Supercond. 28 (2017) 2500105.
[2] V. Gupta, B. Yelamanchili, S. Zou, T. Isaacs-Smith, J.A. Sellers, D.B. Tuckerman, M. C. Hamilton, Thin-film Nb/polyimide superconducting stripline flexible cables, IEEE Trans. Appl. Supercond. 29 (2019) 8664094.
[3] S. Ohya, B. Chiaro, A. Megrant, C. Nei, R. Barends, Y. Chen, J. Kelly, D. Low, J. Mutus, P.J.J. O'Malley, Room temperature deposition of sputtered TiN films for superconducting coplanar waveguide resonators, Supercond. Sci. Technol. 27 (2014), 015009. https://doi.org/10.1088/0953-2048/27/1/015009.
[4] S. Chaudhuri, M.R. Nevala, I.J. Maasilta, Niobium nitride-based normal metal-insulator-superconductor tunnel junction microthermometer, Appl. Phys. Lett. 102 (2013) 132601. https://doi.org/10.1063/1.4800440.
[5] R. Baskaran, A.V. Thanikai Arasu, E.P. Amaladass, L.S. Vaidhyanathan, D. K. Baisnab, Increased upper critical field for nanocrystalline Mon thin films deposited on AlN buffered substrates at ambient temperature, J. Phys. D. 49 (2016) 205304–205307.
[6] A. Fuertes, Chemistry and applications of oxynitride perovskites, J. Mater. Chem. 22 (2012) 3293–3299, https://doi.org/10.1039/C2JM13182J.
[7] J. Goupy, P. Djemia, S. Pouget, L. Belliard, G. Abadias, J.C. Villégier, J. L. Sauvageot, C. Pigot, Structure, electrical conductivity, critical superconducting temperature and mechanical properties of TiNxOy thin films, Surf. Coat. Technol. 237 (2013) 196–204, https://doi.org/10.1016/j.surfcoat.2013.09.019.
[8] Melita Sluban, et al., Controlling disorder and superconductivity in titanium oxynitride nanoribbons with anion exchange, ACS Nano 9 (2015) 10133–10141. https://doi.org/10.1021/acsnano.5b03742.
[9] Kota Tateno, Yuj Masubuchi, Kikkawa Shinichi, Niobium oxynitrides with defective rock salt-type structures, J. Alloy. Comp. 803 (2019) 678–683. https://doi.org/10.1016/j.jallcom.2019.06.320.
[10] K. Inzani, M. Nematollahi, F. Vullum-Bruer, T. Grande, T.W. Reenaasb, S. M. Selbach, Electronic properties of reduced molybdenum oxides, Phys. Chem. Chem. Phys. 19 (2017) 9232–9245. https://doi.org/10.1039/C7CP00644F.
[11] R.S. Patil, M.D. Uplane, P.S. Patil, Structural and optical properties of electrodeposited molybdenum oxide thin films, Appl. Surf. Sci. 252 (2006) 8050–8056. https://doi.org/10.1016/j.apsusc.2005.10.016.
[12] Zhong Cheng Xiang, Qin Zhang, Zhong Zhang, Jin Xi, Qing Xua, Bao Wang, Preparation and photoelectric properties of semiconductor MoO_2 micro/nanospheres with wide bandgap, Ceram. Int. 41 (2015) 977–981. https://doi.org/10.1016/j.ceramint.2014.09.017.
[13] Isabela Alves de Castro, Robi Shankar Datta, Jian Zhen Ou, Castellanos-Gomez Andres, Sharath Sriram, Torben Daeneke, Kourosh Kalantar-zadeh, Molybdenum oxides – from fundamentals to functionality, Adv. Mater. 29 (2017) 1701619. https://doi.org/10.1002/adma.201701619.
[14] Alehdaghi Hassan, Maziar Marandi, Irajizad Azam, Nima Taghavinia, d Jin Jang, Hakimeh Zare, Investigating the different conditions on solution processed MoO_x thin film in long lifetime fluorescent polymer light emitting diodes, Mater. Chem. Phys. 204 (2018) 262–268, https://doi.org/10.1016/j.matchemphys.2017.10.051.
[15] B.T. Matthias, J.K. Hulm, A search for new superconducting compounds, Phys. Rev. 87 (1952) 799–806. https://doi.org/10.1103/PhysRev.87.799.
[16] Kei Inumaru, Kazuya Baba, Shoji Yamanaka, Synthesis and characterization of superconducting β-Mo_2N crystalline phase on a Si substrate: an application of pulsed laser deposition to nitride chemistry, Chem. Mater. 17 (2005) 5935–5940. https://doi.org/10.1021/cm050708i.
[17] Hanlu Zhang, et al., Self-assembled *c*-axis oriented δ-Mon thin films on Si substrates by chemical solution deposition: growth, transport and superconducting, J. Alloy. Comp. 704 (2017) 453–458. https://doi.org/10.1016/j.jallcom.2017.02.084.
[18] N. Haberkorn, S. Bengio, S. Suárez, P.D. Pérez, M. Sirena, J. Guimpel, Effect of the nitrogen-argon gas mixtures on the superconductivity properties of reactively sputtered molybdenum nitride thin films, Mater. Lett. 215 (2018) 15–18. https://doi.org/10.1016/j.matlet.2017.12.045.
[19] N. Haberkorn, S. Bengio, S. Suárez, P.D. Pérez, J.A. Hofer, M. Sirena, Effect of thermal annealing and irradiation damage on the superconducting critical temperature of nanocrystalline γ-Mo_2N thin films, Mater. Lett. 236 (2019) 252–255. https://doi.org/10.1016/j.matlet.2018.10.094.
[20] Juyun Park, Yong-Cheol Kang, Surface characterization of Mo oxynitride films obtained by RF sputtering at various N_2 ratios, Met. Mater. Int. 19 (2013) 55–60. https://doi.org/10.1007/s12540-013-1010-9.
[21] Dan Ruan, Rui Lin, Kui Jiang, Yu Xiang, Yaofeng Zhu, Yaqin Fu, Zilong Wang, Yan He, Wenjie Mai, High-performance porous molybdenum oxynitride based fiber supercapacitors, ACS Appl. Mater. Interfaces 9 (2017) 29699–29706. https://doi.org/10.1021/acsami.7b07522.
[22] O. Nakamura, Eric E. Fullerton, J. Guimpel, Ivan K. Schuller, High T_c thin films with roughness smaller than one unit cell, Appl. Phys. Lett. 60 (1992) 120–122. https://doi.org/10.1063/1.107343.
[23] Andrew H. Simon, in: Handbook of Thin Film Deposition, third, 2012, pp. 55–88.
[24] N. Haberkorn, S. Bengio, H. Troiani, S. Suárez, P.D. Perez, P. Granell, F. Golmar, M. Sirena, J. Guimpel, Thickness dependence of the superconducting properties of γ- Mo_2N thin films on Si (001) grown by DC sputtering at room temperature, Mater. Chem. Phys. 204 (2018) 48–57. https://doi.org/10.1016/j.matchemphys.2017.10.015.
[25] Geug-Tae Kim, Tae-Keun Park, Hongsuk Chung, Young-Tae Kim, Moo-Hyun Kwon, Jeong-Gil Choi, Growth and characterization of chloronitroaniline crystals for optical parametric oscillators: I. XPS study of Mo-based compounds, Appl. Surf. Sci. 152 (1999) 35–43. https://doi.org/10.1016/S0169-4332(99)00293-7.
[26] Baltrusaitisa Jonas, Beatriz Mendoza-Sanchez, Vincent Fernandez, Rick Veenstrab, Nijole Dukstiene, Adam Roberts, Fairley Neal, Generalized molybdenum oxide surface chemical state XPS determination via informed amorphous sample model, Appl. Surf. Sci. 326 (2015) 151–161. https://doi.org/10.1016/j.apsusc.2014.11.077.
[27] D.O. Scanlon, Graeme W. Watson, D.J. Payne, G.R. Atkinson, R.G. Egdell, D.S. L. Law, Theoretical and experimental study of the electronic structures of MoO_3 and MoO_2, J. Phys. Chem. C 114 (2010) 4636–4645. https://doi.org/10.1021/jp9093172.
[28] N.R. Werthamer, E. Helfand, P.C. Hohenberg, Temperature and purity dependence of the superconducting critical field, H_{c2}. III, electron spin spin-orbit effects, Phys. Rev. 147 (1966) 295–302. https://doi.org/10.1103/PhysRev.147.295.
[29] K. Maki, Effect of pauli paramagnetism on magnetic properties of high-field superconductors, Phys. Rev. 148 (1966) 362–369. https://doi.org/10.1103/PhysRev.148.362.
[30] M. Tinkham, Introduction to Superconductivity, second ed., McGraw-Hill, 1996.
[31] I.S. Beloborodov, A.V. Lopatin, V.M. Vinokur, K.B. Efetov, Rev. Mod. Phys. 79 (2007) 469–518. https://doi.org/10.1103/RevModPhys.79.469.
[32] Chiashain Chuang, R.K. Puddy, Huang-De Lin, Shun-Tsung Lo, T.-M. Chen, C. G. Smith, C.-T. Liang, Experimental evidence for Efros–Shklovskii variable range hopping in hydrogenated graphene, Solid State Commun. 152 (2012) 905–908. https://doi.org/10.1016/j.ssc.2012.02.002.

[33] S. Ravi, M. Kar, Study of magneto-resistivity in $La_{1-x}Ag_xMnO_3$ compounds, Phys. B Condens. Matter 348 (2004) 169–176. https://doi.org/10.1016/j.physb.2003.11.087.

[34] Yung-Lung Huang, Shao-Pin Chiu, Zhi-Xin Zhu, Zhi-Qing Li, Juhn-Jong Lin, Variable-range-hopping conduction processes in oxygen deficient polycrystalline ZnO films, J. Appl. Phys. 107 (2010), 063715. https://doi.org/10.1063/1.3357376 7.

[35] Tarsame S. Sian, G.B. Reddy, Optical, structural and photoelectron spectroscopic studies on amorphous and crystalline molybdenum oxide thin films, Sol. Energy Mater. Sol. Cells 82 (2004) 375–386. https://doi.org/10.1016/j.solmat.2003.12.007.